



CHORUS

This is the accepted manuscript made available via CHORUS. The article has been published as:

Noniterative finite amplitude methods for $\langle m \rangle$ and $\langle M \rangle$ giant resonances

Hirokazu Sasaki, Toshihiko Kawano, and Ionel Stetcu

Phys. Rev. C **105**, 044311 — Published 14 April 2022

DOI: [10.1103/PhysRevC.105.044311](https://doi.org/10.1103/PhysRevC.105.044311)

Non-iterative finite amplitude methods for E1 and M1 giant resonances

Hirokazu Sasaki,^{1,*} Toshihiko Kawano,¹ and Ionel Stetcu¹

¹*Theoretical Division, Los Alamos National Laboratory, Los Alamos, New Mexico 87545, USA*

(Dated: March 28, 2022)

The finite amplitude method (FAM) is a very efficient approach for solving the fully self-consistent random-phase approximation (RPA) equations. We use FAM to rederive the RPA matrices for Skyrme functionals, calculate the electric dipole (E1) and the magnetic dipole (M1) giant resonances, and compare the results with available experimental and evaluated data. For the E1 transitions in heavy nuclei, the calculations reproduce well the resonance energy of the photoabsorption cross sections. In the case of M1 transitions, we show that the residual interaction does not affect the transition strength of double-magic nuclei, which suggests that the spin terms in the Skyrme force currently neglected in the present computation could improve the agreement between FAM and experimental data.

I. INTRODUCTION

Giant resonances are collective motions of many neutrons and protons in the atomic nucleus induced by weak external perturbations [1]. The electric dipole resonance (GDR) was first observed by Bothe and Gentner in their photo-absorption experiments [2]. Since then, various types of giant resonances are found in nuclear experiments [1, 3, 4]. Because of the time-reversal invariance in the compound nucleus reaction, strengths of the electric dipole (E1) and the magnetic dipole (M1) excitations are translated into the photon emission process, namely the neutron capture cross sections [5, 6], where an implicit Brink-Axel hypothesis [7] is always assumed. The obtained capture cross sections can be applied to nucleosynthesis calculations in explosive astrophysical sites. It is theoretically predicted that large numbers of unstable nuclei are produced through nucleosynthesis of heavy elements such as the r -process [8–10] and the νp -process [11–13]. The unstable nuclei produced in these processes decay to stable nuclei, and they contribute to a significant fraction of heavy elements in the solar abundance. In induced or spontaneous fission, neutron-rich nuclei far from stability follow the same decay toward stability. Because the experimental data on giant resonances are mainly limited to stable nuclei, the reaction rates on unstable nuclei in nuclear network calculations or fission simulations inevitably depend on the theoretical prediction. Therefore, reliable theoretical calculations of giant resonances are essential to study the origin of heavy elements and not only. In addition, phenomenological models of GDR, which are often employed in calculating the reaction rates for neutron-rich targets, should be validated against more fundamental theoretical models.

As a contemporary theoretical approach, the nuclear density functional theory (DFT) is used to study the properties of the ground and excited states in the nuclear many-body system. Random-phase approximation (RPA) derived from the time-dependent Hartree-

Fock (TDHF) equation can describe dynamical properties of nuclei for external fields [14]. RPA is extended to quasiparticle random-phase approximation (QRPA) by including the pairing correlations [15]. Collective excitations like GDR have been extensively studied in the (Q)RPA calculations [1, 16, 17]. Growing interest includes the M1 transitions, which has been studied in various (Q)RPA approaches [18–25]. Because (Q)RPA is the small amplitude limit of time-dependent DFT, time-dependent Hartree-Fock-Bogoliubov (TDHFB) [26] and time-dependent superfluid local density approximation (TDSLDA) [27] have been also used to calculate giant resonances.

Although DFT-based microscopic approaches have few adjustable parameters, which are usually fitted to masses and select other static properties, solving numerically the QRPA equations is computationally expensive, especially in the case of deformed superfluid nuclei. The finite amplitude method (FAM) is a much less demanding alternative [28–42] to numerically solve the full self-consistent (Q)RPA equations. In FAM calculations, the linear RPA equations are solved iteratively. Because FAM avoids the diagonalization of the large size of (Q)RPA matrices, it reduces the computational costs significantly. FAM was first proposed within the RPA framework [28] and was used to study the E1 transitions [29]. FAM-RPA was soon extended to the QRPA calculations [30] and has been applied to various multipole modes in deformed nuclei [31–34]. There are various applications of the FAM approach, e.g., the extension to the relativistic framework [35, 36] and the construction of RPA matrices in the matrix FAM (m-FAM) [37]. Furthermore, the Skyrme proton-neutron FAM (pnFAM) was applied to the beta-decay [38–40] and the two-neutrino double-beta decay [41]. Finally, FAM-QRPA was also efficiently used to calculate the collective inertia in fission dynamics [42].

In this paper, we analytically derive the contribution of residual interaction in the RPA equations and calculate cross sections of E1 and the M1 transitions. In our implementation of FAM, the residual interaction is explicitly linearized. We chose to solve the RPA matrix equations rather than following an iterative approach, as

* hsasaki@lanl.gov

this involves simply the inversion of a matrix that can be performed numerically very efficiently.

II. THEORY

A. Finite amplitude method (FAM)

We briefly review the formalism of the FAM-RPA calculation following details in Ref. [28, 29]. In the static Hartree-Fock (HF) calculation, we can obtain iteratively the static HF Hamiltonian and the associated single-particle states, $h_0 |\phi_\mu\rangle = \epsilon_\mu |\phi_\mu\rangle$. The single-particle states are divided in occupied (hole) states $\{\phi_i\}$ ($i = 1, \dots, A$) and unoccupied (particle) states $\{\phi_m\}$ ($m = A + 1, \dots$). Hereafter, we use indices i, j for occupied states and m, n for unoccupied states. Nuclear excitations caused by a weak external field can be studied through the time evolution of the one-body density matrix $\rho(t)$ [14]. A time-dependent external field $V_{\text{ext}}(t)$ causes the transition density $\delta\rho(t)$ and the associated residual field $\delta h(t)$. In the frequency space, these are denoted by $V_{\text{ext}}(\omega)$, $\delta\rho(\omega)$, and $\delta h(\omega)$. Assuming a weak external field, the transition density in the ω representation is expressed as

$$\delta\rho(\omega) = \sum_{i=1}^A \{|X_i(\omega)\rangle \langle\phi_i| + |\phi_i\rangle \langle Y_i(\omega)|\}, \quad (1)$$

where $|X_i(\omega)\rangle$ ($|Y_i(\omega)\rangle$) are the forward (backward) amplitudes. From the linear response of the TDHF equations, the linear RPA equations are given by

$$\begin{aligned} \omega |X_i(\omega)\rangle &= (h_0 - \epsilon_i) |X_i(\omega)\rangle \\ &+ \hat{P} \{V_{\text{ext}}(\omega) + \delta h(\omega)\} |\phi_i\rangle, \end{aligned} \quad (2)$$

$$\begin{aligned} -\omega \langle Y_i(\omega)| &= \langle Y_i(\omega)| (h_0 - \epsilon_i) \\ &+ \langle\phi_i| \{V_{\text{ext}}(\omega) + \delta h(\omega)\} \hat{P}, \end{aligned} \quad (3)$$

where $\hat{P} = 1 - \sum_{i=1}^A |\phi_i\rangle \langle\phi_i|$ is the projector onto unoccupied states. In the general framework of FAM, the residual interaction is linearized by a small parameter η and written as

$$\delta h(\omega) = \frac{\hbar(\langle\psi'_i|, |\psi_i\rangle) - h_0}{\eta}, \quad (4)$$

where h is the single-particle Hamiltonian of the TDHF calculation and $|\psi_i\rangle = |\phi_i\rangle + \eta |X_i(\omega)\rangle$, $\langle\psi'_i| = \langle\phi_i| + \eta \langle Y_i(\omega)|$ are the ket and bra representations of the single-particle state of h . The residual interaction in Eq. (4) is obtained numerically by employing the small parameter η and the single-particle state. Equations (2) and (3) are solved iteratively together with Eq. (4).

The FAM calculation is often carried out in the mixed representation [29, 34]. However, in this paper, we solve

the linear RPA equations in the matrix form. The forward and backward amplitudes are decomposed by the unoccupied states [28],

$$|X_i(\omega)\rangle = \sum_{m>A} X_{mi}(\omega) |\phi_m\rangle, \quad (5)$$

$$|Y_i(\omega)\rangle = \sum_{m>A} Y_{mi}^*(\omega) |\phi_m\rangle. \quad (6)$$

In the matrix form, the RPA equations in Eqs. (2) and (3) are described by

$$\begin{aligned} (\epsilon_m - \epsilon_i - \omega) X_{mi}(\omega) &+ \langle\phi_m| \delta h(\omega) |\phi_i\rangle \\ &= -\langle\phi_m| V_{\text{ext}}(\omega) |\phi_i\rangle, \end{aligned} \quad (7)$$

$$\begin{aligned} (\epsilon_m - \epsilon_i + \omega) Y_{mi}(\omega) &+ \langle\phi_i| \delta h(\omega) |\phi_m\rangle \\ &= -\langle\phi_i| V_{\text{ext}}(\omega) |\phi_m\rangle. \end{aligned} \quad (8)$$

In order to simplify the notation, the index ω is dropped hereafter. The external field and the residual interactions are independent of ω in our numerical calculation. In the following discussion, it is assumed that the external field V_{ext} does not change the isospin of the nucleon.

B. RPA equations

The RPA matrices A and B in the well-known RPA equation [14] are derived from the explicit linearization of the TDHF Hamiltonian with the expansion parameter η . Because we work with Skyrme-type nuclear energy density functionals the single-particle Hamiltonian writes [43–46]

$$h = \sum_q h_q = \sum_q (h_q^{\text{even}} + h_q^{\text{odd}}), \quad (9)$$

$$\begin{aligned} h_q^{\text{even}} &= -\vec{\nabla} \cdot \frac{\hbar^2}{2m_q^*} \vec{\nabla} + U_q + \vec{W}_q \cdot (-i) (\vec{\nabla} \times \vec{\sigma}) \\ &+ \delta_{qp} V_{\text{coul}}, \end{aligned} \quad (10)$$

$$h_q^{\text{odd}} = \vec{S}_q \cdot \vec{\sigma} - \frac{i}{2} [(\vec{\nabla} \cdot \vec{A}_q) + 2\vec{A}_q \cdot \vec{\nabla}], \quad (11)$$

$$V_{\text{coul}} = \frac{e^2}{2} \int d^3r' \frac{\rho_p}{|\vec{r} - \vec{r}'|} - \frac{e^2}{2} \left(\frac{3}{\pi}\right)^{1/3} \rho_p^{1/3}, \quad (12)$$

where \vec{r} is the space coordinate and $\vec{\sigma}$ represents the spin of the nucleon q ($q = n$ for neutrons and $q = p$ for protons), while h_q^{even} and h_q^{odd} are the time-even and time-odd Hamiltonian, respectively. The central potential U_q , the effective mass m_q^* , and the spin-orbit potential \vec{W}_q in the time-even Hamiltonian are calculated using the nucleon particle density ρ_q , the kinetic energy density τ_q ,

and the spin-orbit density \vec{J}_q [43, 45]. These local quantities are computed with the single-particle states of the TDHF Hamiltonian $\{\psi_\mu, \psi_\mu^*\}$ (see the detail in Sec. II C). V_{coul} is the Coulomb potential, where ρ_p is the proton density defined in Eq. (20). For even-even nuclei, the time-odd Hamiltonian does not contribute to the static HF calculation because the time-odd fields such as the spin density \vec{s}_q and the current density \vec{j}_q used to compute \vec{S}_q and \vec{A}_q are zero under the time-reversal symmetry [43, 45]. Hence, the single particle states $\{\phi_\mu\}$ are determined solving the eigenvalue equation for h_q^{even} . On the other hand, the density matrix cannot be time-even in the dynamical evolution. The time-odd contribution must be included for even for even-even nuclei in order to satisfy the Galilean invariance [43, 46]. In the FAM-RPA calculation, both time-even and time-odd potentials are expressed as the functions of the self-consistent single particle states without any mixing. According to Eqs. (5), (6), the occupied state and their complex conjugate of the TDHF Hamiltonian in our FAM calculation are expanded by the small parameter η ,

$$\psi_i(\vec{r}, \sigma, q) = \phi_i(\vec{r}, \sigma, q) + \eta \sum_{m \in q} X_{mi}^q \phi_m(\vec{r}, \sigma, q) + \mathcal{O}(\eta^2), \quad (13)$$

$$\psi_i^*(\vec{r}, \sigma, q) = \phi_i^*(\vec{r}, \sigma, q) + \eta \sum_{m \in q} Y_{mi}^q \phi_m^*(\vec{r}, \sigma, q) + \mathcal{O}(\eta^2). \quad (14)$$

For a detailed discussion on how we calculate $\phi_i(\vec{r}, \sigma, q)$ in our numerical implementation, we refer the interested reader to Appendix A. In the limit of $\eta \rightarrow 0$, the residual interaction in Eq. (4) should be independent of η and expressed as linear combinations of coefficients $\{X_{nj}^{q'}\}$ and $\{Y_{nj}^{q'}\}$,

$$\lim_{\eta \rightarrow 0} \delta h = \sum_{q'} \sum_{nj \in q'} X_{nj}^{q'} \left. \frac{\partial h}{\partial(\eta X_{nj}^{q'})} \right|_{\eta=0} + \sum_{q'} \sum_{nj \in q'} Y_{nj}^{q'} \left. \frac{\partial h}{\partial(\eta Y_{nj}^{q'})} \right|_{\eta=0}. \quad (15)$$

In such explicit linearization of the residual interactions, we no longer need the small parameter η and an iterative procedure to solve Eqs. (7) and (8). The expansions of the single-particle states in Eqs. (13) and (14) enable the explicit linearization of the Skyrme potentials. When the external field and the single-particle Hamiltonian are local in the coordinate space, the RPA equations in Eqs. (7) and (8) are described in the matrix form,

$$\left\{ \begin{pmatrix} A & B \\ B^* & A^* \end{pmatrix} - \omega \begin{pmatrix} 1 & 0 \\ 0 & -1 \end{pmatrix} \right\} \begin{pmatrix} X_{nj}^{q'} \\ Y_{nj}^{q'} \end{pmatrix} = - \begin{pmatrix} f_{mi}^q \\ f_{im}^q \end{pmatrix}, \quad (16)$$

$$A_{mi, nj}^{q, q'} = (\epsilon_m - \epsilon_i) \delta_{mn} \delta_{ij} + \int d^3r \phi_m^{q*} \left(\frac{\partial h_q}{\partial(\eta X_{nj}^{q'})} \right)_{\eta=0} \phi_i^q, \quad (17)$$

$$B_{mi, nj}^{q, q'} = \int d^3r \phi_m^{q*} \left(\frac{\partial h_q}{\partial(\eta Y_{nj}^{q'})} \right)_{\eta=0} \phi_i^q, \quad (18)$$

$$f_{mi}^q = \int d^3r \phi_m^{q*} V_{\text{ext}} \phi_i^q, \quad f_{im}^q = \int d^3r \phi_i^{q*} V_{\text{ext}} \phi_m^q, \quad (19)$$

where the limit in Eq. (15) is used to configure the elements of RPA matrices in Eqs. (17) and (18). In the equations above, we use a simple notation, $\phi_\mu^q \equiv \phi_\mu(\vec{r}, \sigma, q)$. The matrices $A_{mi, nj}^{q, q'}$ and $B_{mi, nj}^{q, q'}$ are functions of ϕ_i^q , ϕ_m^{q*} , $\phi_j^{q'}$, and $\phi_n^{q'}$ with the various Skyrme parameters [47]. A detailed description of the RPA matrices A and B is given below.

The argument for solving iteratively the FAM equations is the size of the matrices A and B , which is significant in the case of QRPA, especially for deformed nuclei. While this is correct, one can also argue that extremely efficient numerical methods are available for inverting large matrices, especially if one uses a parallel algorithm. Thus, while we chose to use complex ω , like in the other FAM-based approaches, we calculate explicitly the A and B matrices and by direct inversion, we solve for the amplitudes X and Y in Eq. (16). Since A and B are given at a one-time cost, the approach will most likely compete with iterative FAM.

C. The residual interaction of h_q^{even}

The RPA matrices A and B are composed of local densities and currents given by the single-particle states of the HF calculation. In our RPA calculation, the effective mass m_q^* and potentials such as U_q and W_q in the time-even Hamiltonian are obtained from the nucleon density ρ_q , the kinetic energy density τ_q , and the spin-orbit density \vec{J}_q defined as [48],

$$\rho_q = \sum_{i \in q} \psi_i^{q*} \psi_i^q, \quad (20)$$

$$\tau_q = \sum_{i \in q} \vec{\nabla} \psi_i^{q*} \cdot \vec{\nabla} \psi_i^q, \quad (21)$$

$$\vec{J}_q = -i \sum_{i \in q} \psi_i^{q*} (\vec{\nabla} \times \vec{\sigma}) \psi_i^q, \quad (22)$$

where $\psi_i^q \equiv \psi_i(\vec{r}, \sigma, q)$ and $\psi_i^{q*} \equiv \psi_i^*(\vec{r}, \sigma, q)$ are the wave functions in Eqs. (13) and (14), respectively. The index i in the sums represents the occupied states of nucleon q . The summation of the spin dependence of wave functions can be done automatically in Eqs. (20)-(22), when the ϕ_μ^q is composed of both the spin-up state

$\chi_{1/2}(\sigma)$ and the spin-down state $\chi_{-1/2}(\sigma)$. In fact, as shown in Eq. (A1), the HF single-particle state used in our numerical calculation includes both the spin-up and spin-down states. The contribution of h_q^{even} on the RPA matrices in Eqs. (17) and (18) is described by the partial derivatives of Eqs. (20)–(22). According to Eqs. (13) and (14), the time-even fields in Eqs. (20)–(22) are expanded by η . In the limit of $\eta \rightarrow 0$, partial derivatives such as $\partial/\partial(\eta X_{nj})$ and $\partial/\partial(\eta Y_{nj})$ of the time-even fields are derived analytically,

$$\left(\frac{\partial \rho_q}{\partial(\eta X_{nj}^{q'})} \right)_{\eta=0} = \delta_{qq'} \phi_j^{q*} \phi_n^q, \quad (23)$$

$$\left(\frac{\partial \tau_q}{\partial(\eta X_{nj}^{q'})} \right)_{\eta=0} = \delta_{qq'} \vec{\nabla} \phi_j^{q*} \cdot \vec{\nabla} \phi_n^q, \quad (24)$$

$$\left(\frac{\partial(\vec{\nabla} \cdot \vec{J}_q)}{\partial(\eta X_{nj}^{q'})} \right)_{\eta=0} = \delta_{qq'} (-i) \vec{\nabla} \phi_j^{q*} \cdot (\vec{\nabla} \times \vec{\sigma}) \phi_n^q, \quad (25)$$

$$\left(\frac{\partial \rho_q}{\partial(\eta Y_{nj}^{q'})} \right)_{\eta=0} = \delta_{qq'} \phi_n^{q*} \phi_j^q, \quad (26)$$

$$\left(\frac{\partial \tau_q}{\partial(\eta Y_{nj}^{q'})} \right)_{\eta=0} = \delta_{qq'} \vec{\nabla} \phi_n^{q*} \cdot \vec{\nabla} \phi_j^q, \quad (27)$$

$$\left(\frac{\partial(\vec{\nabla} \cdot \vec{J}_q)}{\partial(\eta Y_{nj}^{q'})} \right)_{\eta=0} = \delta_{qq'} (-i) \vec{\nabla} \phi_n^{q*} \cdot (\vec{\nabla} \times \vec{\sigma}) \phi_j^q, \quad (28)$$

where ϕ_j^q and ϕ_n^q are occupied and unoccupied single-particle states, respectively. Since the external field V_{ext} we consider here does not change the isospins of nucleons, Eqs. (23)–(28) should be zero when $q \neq q'$. The divergence of \vec{J}_q has a contribution to the Skyrme potentials [48]. After simple algebra, we can show that Eqs. (26)–(28) are complex conjugates of Eqs. (23)–(25). Such a property of the complex conjugate in the partial derivatives in the backward amplitudes is also confirmed in the time-odd Hamiltonian. Therefore, the RPA matrix B is given by the complex conjugate of the partial derivative

with respect to the forward amplitude,

$$B_{mi,nj}^{q,q'} = \int d^3r \phi_m^{q*} \left(\frac{\partial h_q}{\partial(\eta X_{nj}^{q'})} \right)_{\eta=0}^* \phi_i^q. \quad (29)$$

It is enough to calculate the partial derivative $\partial h_q/\partial(\eta X_{nj}^{q'})|_{\eta=0}$ only to derive the RPA matrix B . Hereafter, we mainly focus on the derivation of the RPA matrix A . The Skyrme forces are parameterized by the t and x coefficients [47]. We follow the detailed description of Skyrme potentials in the form of b coefficients [45]. We can calculate the contribution of the time-even potentials to the RPA matrix A by using Eqs. (23)–(25). For example, the contribution of the effective mass m_q^* on the RPA matrix A is given by

$$\begin{aligned} & \int d^3r \phi_m^{q*} \vec{\nabla} \cdot \left(\frac{\partial}{\partial(\eta X_{nj}^{q'})} \frac{-\hbar^2}{2m_q^*} \right)_{\eta=0} \vec{\nabla} \phi_i^q \\ &= - \int d^3r \phi_m^{q*} \vec{\nabla} \cdot \left\{ b_1 \frac{\partial(\rho_n + \rho_p)}{\partial(\eta X_{nj}^{q'})} - b'_1 \frac{\partial \rho_q}{\partial(\eta X_{nj}^{q'})} \right\}_{\eta=0} \vec{\nabla} \phi_i^q \\ &= (b_1 - \delta_{qq'} b'_1) \int d^3r \phi_j^{q'*} \phi_n^{q'} \vec{\nabla} \phi_m^{q*} \cdot \vec{\nabla} \phi_i^q, \end{aligned} \quad (30)$$

where the term $\vec{\nabla} \phi_m^{q*}$ in the third line comes from integration by parts. b_1 and b'_1 are coefficients in the effective mass [45]. In the same way, the contribution of the spin-orbit potential is given by

$$\begin{aligned} & \int d^3r \phi_m^{q*} \left(\frac{\partial \vec{W}_q}{\partial(\eta X_{nj}^{q'})} \right)_{\eta=0} \cdot (-i) (\vec{\nabla} \times \vec{\sigma}) \phi_i^q \\ &= -(b_4 + \delta_{qq'} b'_4) \int d^3r \phi_j^{q'*} \phi_n^{q'} \vec{\nabla} \phi_m^{q*} \cdot (-i) (\vec{\nabla} \times \vec{\sigma}) \phi_i^q, \end{aligned} \quad (31)$$

where the second line is derived from the integration by parts and the property of $\vec{\nabla} \cdot (\vec{\nabla} \times \vec{\sigma}) = 0$. We calculate the partial derivatives of the central and the Coulomb potentials as Eqs. (30) and (31). Finally, the contribution of h_q^{even} to the RPA matrix A in Eq. (17) is described by

$$\begin{aligned}
& \int d^3r \phi_m^{q*} \left(\frac{\partial h_q^{\text{even}}}{\partial(\eta X_{nj}^{q'})} \right)_{\eta=0} \phi_i^q = (b_0 - \delta_{qq'} b'_0) \int d^3r \phi_m^{q*} \phi_i^q \phi_j^{q'*} \phi_n^{q'} \\
& + (b_1 - \delta_{qq'} b'_1) \int d^3r \left(\phi_m^{q*} \phi_i^q \vec{\nabla} \phi_j^{q'*} \cdot \vec{\nabla} \phi_n^{q'} + \phi_j^{q'*} \phi_n^{q'} \vec{\nabla} \phi_m^{q*} \cdot \vec{\nabla} \phi_i^q \right) \\
& - (b_2 - \delta_{qq'} b'_2) \int d^3r \left\{ \phi_m^{q*} \phi_i^q \left(\phi_j^{q'*} \nabla^2 \phi_n^{q'} + \phi_n^{q'} \nabla^2 \phi_j^{q'*} + 2 \nabla \phi_j^{q'*} \cdot \nabla \phi_n^{q'} \right) \right\} \\
& + b_3 \int d^3r \left\{ \frac{(\alpha+2)(\alpha+1)}{3} (\rho_0)^\alpha \phi_m^{q*} \phi_i^q \phi_j^{q'*} \phi_n^{q'} \right\} \\
& - b'_3 \int d^3r \left[\left\{ \frac{2\alpha}{3} (\rho_0)^{\alpha-1} (\rho_{0,q} + \rho_{0,q'}) + \frac{2}{3} (\rho_0)^\alpha \delta_{qq'} + \frac{\alpha(\alpha-1)}{3} (\rho_0)^{\alpha-2} \sum_{q''} (\rho_{0,q''})^2 \right\} \phi_m^{q*} \phi_i^q \phi_j^{q'*} \phi_n^{q'} \right] \\
& - (b_4 + \delta_{qq'} b'_4) \int d^3r \left\{ \phi_m^{q*} \phi_i^q \vec{\nabla} \phi_j^{q'*} \cdot (-i) (\vec{\nabla} \times \vec{\sigma}) \phi_n^{q'} + \phi_j^{q'*} \phi_n^{q'} \vec{\nabla} \phi_m^{q*} \cdot (-i) (\vec{\nabla} \times \vec{\sigma}) \phi_i^q \right\} \\
& + \delta_{qp} \delta_{q'p} \frac{e^2}{2} \int d^3r \left\{ \phi_m^{q*} \phi_i^q \left(\int d^3r' \frac{\phi_j^{q'*} \phi_n^{q'}}{|\vec{r}' - \vec{r}'|} \right) - \frac{1}{3} \left(\frac{3}{\pi} \right)^{1/3} (\rho_{0,p})^{-2/3} \phi_m^{q*} \phi_i^q \phi_j^{q'*} \phi_n^{q'} \right\}, \tag{32}
\end{aligned}$$

where $\rho_0 = \rho_{0,n} + \rho_{0,p}$ is the summation of the density of nucleon, $\rho_{0,q} = \sum_{i \in q} \phi_i^{q*} \phi_i^q$ ($q = n, p$). b_i, b'_i ($i = 0, 1, 2, 3$, and 4) and α are the parameters in the Skyrme forces [45]. It is clear from Eq. (32) that the residual interaction of h_q^{even} is composed of the single-particle states of the static HF calculation without any forward and backward amplitudes. We show the detailed descriptions of integrands such as $\phi_m^{q*} \phi_i^q$, $\vec{\nabla} \phi_m^{q*} \vec{\nabla} \phi_i^q$, $\phi_j^{q'*} \nabla^2 \phi_n^{q'}$, and $(-i) \vec{\nabla} \phi_m^{q*} (\vec{\nabla} \times \vec{\sigma}) \phi_i^q$ in Appendix A. The first term in the last line of Eq. (32) represents the contribution from the direct term of Coulomb potential. We discuss the calculation method for the double spatial integrals of the direct term in Appendix B.

D. The residual interaction of h_q^{odd}

The time-odd Hamiltonian h_q^{odd} itself is a time-even field, but this Hamiltonian is composed of time-odd fields such as the spin density \vec{s}_q and the current density \vec{j}_q [43, 45]. The time-odd fields of nucleon q are described by

$$\vec{s}_q = \sum_{i \in q} \psi_i^{q'*} \vec{\sigma} \psi_i^q, \tag{33}$$

$$\vec{j}_q = \frac{1}{2i} \sum_{i \in q} \left\{ \psi_i^{q'*} \vec{\nabla} \psi_i^q - \psi_i^q \vec{\nabla} \psi_i^{q'*} \right\}. \tag{34}$$

In the limit of $\eta \rightarrow 0$, the time-odd fields in the equations above are converged to zero when the time-reversal

symmetry is satisfied in the HF calculation. As done in the time-even fields, We can expand Eqs. (33) and (34) by using Eqs. (13) and (14). Then, we obtain the partial derivatives of these time-odd fields,

$$\left(\frac{\partial \vec{s}_q}{\partial(\eta X_{nj}^{q'})} \right)_{\eta=0} = \delta_{qq'} \phi_j^{q'*} \vec{\sigma} \phi_n^{q'}, \tag{35}$$

$$\left(\frac{\partial \vec{j}_q}{\partial(\eta X_{nj}^{q'})} \right)_{\eta=0} = \delta_{qq'} \frac{1}{2i} \left(\phi_j^{q'*} \vec{\nabla} \phi_n^{q'} - \phi_n^{q'} \vec{\nabla} \phi_j^{q'*} \right), \tag{36}$$

$$\left(\frac{\partial \vec{s}_q}{\partial(\eta Y_{nj}^{q'})} \right)_{\eta=0} = \delta_{qq'} \phi_n^{q'} \vec{\sigma} \phi_j^{q'*}, \tag{37}$$

$$\left(\frac{\partial \vec{j}_q}{\partial(\eta Y_{nj}^{q'})} \right)_{\eta=0} = \delta_{qq'} \frac{1}{2i} \left(\phi_n^{q'} \vec{\nabla} \phi_j^{q'*} - \phi_j^{q'*} \vec{\nabla} \phi_n^{q'} \right), \tag{38}$$

where Eqs. (37) and (38) are the complex conjugates of Eqs. (35) and (36). As discussed in Sec.II C, such the complex conjugate relations lead to the property of the RPA matrix B in Eq. (29). The time-odd potentials such as \vec{S}_q and \vec{A}_q in h_q^{odd} are composed of the time-odd fields in Eqs. (33) and (34). The detail of these potentials is shown in Ref. [45]. By using Eqs. (11), (35), and (36), the partial derivative of h_q^{odd} in the RPA matrix A is derived;

$$\begin{aligned}
& \int d^3r \phi_m^{q*} \left(\frac{\partial h_q^{\text{odd}}}{\partial(\eta X_{nj}^{q'})} \right)_{\eta=0} \phi_i^q \\
&= \int d^3r \left\{ \frac{\partial \vec{S}_q}{\partial(\eta X_{nj}^{q'})} \cdot (\phi_m^{q*} \vec{\sigma} \phi_i^q) + \frac{\partial \vec{A}_q}{\partial(\eta X_{nj}^{q'})} \cdot \frac{1}{2i} (\phi_m^{q*} \vec{\nabla} \phi_i^q - \phi_i^q \vec{\nabla} \phi_m^{q*}) \right\}_{\eta=0} \\
&= -2(b_1 - \delta_{qq'} b'_1) \int d^3r \left\{ \frac{1}{2i} (\phi_m^{q*} \vec{\nabla} \phi_i^q - \phi_i^q \vec{\nabla} \phi_m^{q*}) \cdot \frac{1}{2i} (\phi_j^{q'*} \vec{\nabla} \phi_n^{q'} - \phi_n^{q'} \vec{\nabla} \phi_j^{q'*}) \right\} \\
&\quad - (b_4 + \delta_{qq'} b'_4) \int d^3r \left\{ \frac{1}{2i} (\phi_m^{q*} \vec{\nabla} \phi_i^q - \phi_i^q \vec{\nabla} \phi_m^{q*}) \cdot \vec{\nabla} \times (\phi_j^{q'*} \vec{\sigma} \phi_n^{q'}) + \frac{1}{2i} (\phi_j^{q'*} \vec{\nabla} \phi_n^{q'} - \phi_n^{q'} \vec{\nabla} \phi_j^{q'*}) \cdot \vec{\nabla} \times (\phi_m^{q*} \vec{\sigma} \phi_i^q) \right\}, \quad (39)
\end{aligned}$$

where the integration by parts is done in the term of \vec{A}_q from the first line to the second one. The detailed descriptions of the integrands in our numerical calculation are given in Appendix A.

Finally, the matrices in Eqs. (17) and (18) are derived from Eqs. (29), (32), and (39). From these equations, we can also confirm that these matrices are Hermitian ($A_{mi,nj}^{q,q'} = A_{nj,mi}^{q',q}$) and symmetric ($B_{mi,nj}^{q,q'} = B_{nj,mi}^{q',q}$), which is consistent with the general property of the RPA matrices [14]. The RPA matrices do not include X_{mi}^q , and Y_{mi}^q , so that the forward and backward amplitudes are obtained by solving Eq. (16) without the need for an iterative procedure.

Note that all the RPA equations given above are in the matrix form. The same linearization could be also applied to the mixed representation [29].

Extension of non-iterative FAM-RPA to FAM-QRPA is straightforward by employing the same technique described by Avogadro and Nakatsukasa [30]. This certainly increases the number of particle-hole configurations. However, they are important only for the states with low excitation energies near the Fermi surface. We limit ourselves to FAM-RPA in this paper.

E. External fields for E1 and M1 transitions

The calculated results of FAM-RPA can be compared with experimental data of the photoabsorption cross section. Here, we use a complex frequency, $\omega = E + i\gamma/2$. E and γ correspond to the energy of the incoming photon and the Lorentzian width. This γ parameter characterizes the width of the photoabsorption cross section. The transition strength is described by the forward and backward amplitudes [28],

$$\frac{dB(E; V_{\text{ext}})}{dE} = -\frac{1}{\pi} \text{Im} \sum_q \sum_{m,i \in q} (f_{mi}^{q*} X_{mi}^q + f_{im}^{q*} Y_{mi}^q). \quad (40)$$

As the external field, we consider the electric and magnetic dipole operators that induce E1 and M1 transitions.

The electric dipole operator is written as the spherical harmonics of neutrons and protons,

$$D_K = \sum_{i=1}^A e_{\text{eff}}^{(i)} r_i Y_{1K}(\theta_i, \varphi_i) \quad (K = 0, \pm 1), \quad (41)$$

where $e_{\text{eff}}^{(i)} \equiv -eZ/A$ (eN/A) for neutrons (protons). The $(r_i, \theta_i, \varphi_i)$ represents the spherical coordinate of nucleon i . The photoabsorption cross section of E1 transition is given by [14, 29],

$$\sigma_{\text{abs}}(E; \text{E1}) = \frac{16\pi^3}{9\hbar c} E \sum_{K=0,\pm 1} \frac{dB(E; D_K)}{dE}, \quad (42)$$

where we impose $V_{\text{ext}} = \sum_{K=0,\pm 1} D_K$ on Eq. (40). In the case of M1 transition, the magnetic dipole operator is represented by operators of a spin part $\vec{\sigma}_i/2$ and an orbital part $\vec{l}_i = -i(\vec{r}_i \times \vec{\nabla}_i)$ of nucleon i ,

$$M_K = \mu_N \sum_{i=1}^A \left(g_s^{(i)} \frac{\vec{\sigma}_i}{2} + g_l^{(i)} \vec{l}_i \right) \cdot \vec{\nabla} (r_i Y_{1K}(\theta_i, \varphi_i)) \quad (K = 0, \pm 1), \quad (43)$$

where μ_N is the nuclear magneton. The g factors are $g_s^{(i)} = -3.826(5.586)$ and $g_l^{(i)} = 0(1)$ for neutrons (protons). Similar to the case of the E1 transition, the cross section of M1 transition can be expressed as

$$\sigma_{\text{abs}}(E; \text{M1}) = \frac{16\pi^3}{9\hbar c} E \sum_{K=0,\pm 1} \frac{dB(E; M_K)}{dE}. \quad (44)$$

We note that, for the numerical calculation, we employ the single-particle states labeled in the cylindrical coordinate. Therefore, the spherical coordinates of nucleons in Eqs. (41) and (43) should be transformed to the cylindrical coordinate when the coefficients in Eq. (19) are calculated (see the detail in Appendix C).

III. RESULTS AND DISCUSSIONS

A. E1 transition

1. Benchmark calculation

The photoabsorption cross sections of both E1 and M1 transitions are calculated based on the RPA equations as given in Sec. II. The RPA calculations use the single-particle states of the HF+BCS calculation. The BCS calculation is required to include the pairing correlation in the HF single-particle state for deformed nuclei. The HF+BCS calculation is the same as in work by Bonneau *et al.* [49], where the single particle wave functions are expanded in the axially symmetric harmonic oscillator basis [48], and we solve the BCS gap equation. Deformation parameters are taken from Table 1 of Ref. [50] to start the iterative procedure. With these initial deformation parameters, we can achieve very fast convergence. In the HF+BCS calculation, we employ the parameterization of SLy4 [47] for Skyrme interactions. We focus on even-even nuclei whose HF equations satisfy the time-reversal symmetry. The detailed description of the single-particle state in the cylindrical coordinate is given in Appendix A.

We apply the technique discussed above to a wide mass range of nuclei in order to calculate the cross section of the E1 transition. We solve Eq. (16) for the photon energies starting from $E = 0.5$ MeV at every 250 keV.

Here, we determine the size of the configuration space of the unoccupied states by imposing a cutoff energy E_{cut} measured from the Fermi energy surface. We consider the unoccupied state of nucleon q whose single-particle energy satisfies: $\epsilon_m < E_{\text{cut}} + \epsilon_{i,q,\text{max}}$, where the $\epsilon_{i,q,\text{max}}$ is the maximum energy of the occupied states of neutron ($q = n$) or proton ($q = p$).

Figure 1(a) shows the sensitivity of the E_{cut} to the E1 cross section of ^{40}Ca . The Lorentzian width is $\gamma = 2$ MeV in $K = 0, \pm 1$. As shown by the almost identical dash-dotted and dashed lines, we can safely say that the calculation converges when $E_{\text{cut}} > 30$ MeV. When we increase E_{cut} , the tail on the higher side of GDR becomes larger, because more energetically higher unoccupied states are involved, although these transitions are weak.

The energy-weighted sum rule m_1 [34] can be estimated by integrating the photoabsorption cross section. For $E_{\text{cut}} = 30$ MeV (dash-dotted line), the integration up to $E = 40$ MeV yields $m_1 = 161.8 e^2 \text{fm}^2 \text{MeV}$. The energy-weighted sum rule exhausts 93% of the value computed from the HF ground-state density [34],

$$m_1 = \sum_{K=0,\pm 1} m_1(D_K) = (1 + \kappa) \frac{e^2 \hbar^2}{2m} \frac{NZ}{A} \frac{9}{4\pi}, \quad (45)$$

$$\kappa = \frac{2m}{\hbar^2} b_1 \frac{A}{NZ} \int d^3r \rho_{0,n} \rho_{0,p}, \quad (46)$$

where b_1 is one of the coefficients of Skyrme parameteri-

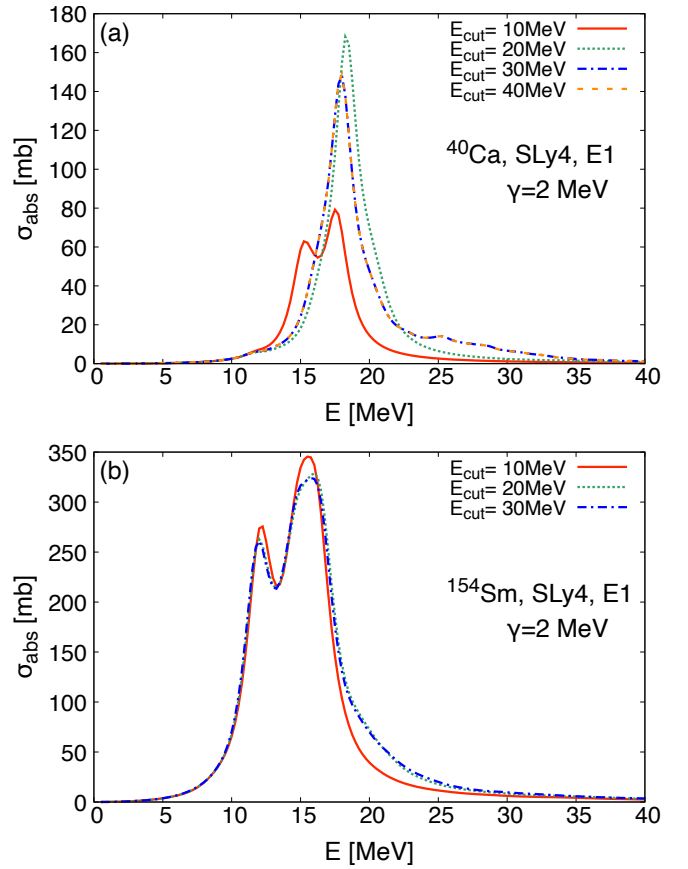


FIG. 1. The calculated GDR cross sections in Eq. (42) for (a) ^{40}Ca and (b) ^{154}Sm with different energy cutoff E_{cut} . The Lorentzian width is fixed to $\gamma = 2$ MeV.

zation and $\kappa = 0.16$ is the enhancement factor for ^{40}Ca . Adding the high-energy region ($E > 40$ MeV) to the integration, the sum rule is better reproduced. The value of κ reflects the contribution from many-body interactions and depends on the model of the Skyrme forces employed.

In the case of heavy nuclei ($A > 150$), as shown in Fig. 1(b), the convergence for E_{cut} is faster, since the single-particle state density becomes higher. For $E_{\text{cut}} = 20$ MeV (dotted line), the m_1 estimated from the energy integration of the cross section exhausts 95% the rhs of Eq.(45) where $\kappa = 0.18$ for ^{154}Sm .

Hereafter, we adopt the cutoff energy, $E_{\text{cut}} = 30$ MeV for light nuclei ($A \leq 150$) and 20 MeV for heavy nuclei ($A > 150$). The resonance energy of GDR becomes lower as the mass number of the nuclei increases [3], so that we perform the RPA calculation for $A \leq 150$ and $A > 150$ up to $E = 40$ MeV and 30 MeV, respectively. Since the Lorentzian width γ is a free parameter in the FAM calculation, we employ the recommended experimental GDR width Γ within the Standard Lorentzian approach in Table III of Ref. [51]. Although the accuracy of the GDR tail region might be suffered by the Lorentzian width used, a different photo-absorption mechanism at higher

energies called the quasi-deuteron absorption [52, 53] brings a larger uncertainty when the calculated results are compared with experimental data. In this sense estimation of the most reasonable width might be better conducted in the peak region of GDR rather than the tail region.

2. Spherical nuclei

Figure 2 shows the cross sections of E1 transitions for spherical nuclei such as ^{16}O , ^{40}Ca , ^{54}Fe , and ^{208}Pb . In the case of spherical nucleus, the transition strength, $dB(E, D_K)/dE$ ($K = 0, \pm 1$) is independent of the value of K . The solid lines show the numerical results of Eq. (42) in our FAM calculations. The symbols are experimental data or evaluated experimental data of the photoabsorption cross section in EXFOR [58]. The error bar is not shown in the evaluated data of ^{208}Pb [57] in Fig. 2(d). The experimental GDR data are often represented by the Lorentzian distribution [3],

$$\sigma_{\text{GDR}}(E) = \frac{\sigma_R}{1 + [(E^2 - E_R^2)^2 / E^2 \Gamma_R^2]}, \quad (47)$$

where σ_R , Γ_R , and E_R are the peak cross section, the full width at half-maximum, and the resonance energy, respectively. The dashed lines in Fig. 2 show the Lorentzian parameterized experimental GDR compiled at IAEA [51].

For the light nuclei, the GDR resonance energy E_R in the FAM calculation tends to be smaller than that of experimental data. In the case of ^{16}O (Fig. 2(a)), E_R is lower by 4.3 MeV. As shown in Fig. 2(b), the deviation of E_R is 2.3 MeV for ^{40}Ca . The discrepancy of the GDR peak is more noticeable in light nuclei. Such disagreement is also seen in the previous RPA calculations [29, 59]. The experimental data of E_R can be explained by the superposition of the Goldhaber-Teller mode that produces the dependence $E_R \propto A^{-1/6}$ and the Steinwedel-Jensen mode that produces $E_R \propto A^{-1/3}$ [3, 60]. The A dependence of E_R in experiments can be fitted by $A^{-1/6}$ for light nuclei. The RPA description underestimates the contribution of the surface mode (Goldhaber-Teller mode), which may imply an insufficient isovector surface energy in the present Skyrme forces [59].

As shown in Figs. 2(c) and 2(d), the deviations between the resonance energy of FAM and that of σ_{GDR} are 0.85 MeV and 0.37 MeV in ^{54}Fe and ^{208}Pb , respectively. Therefore, the discrepancy between the FAM calculations (solid lines) and the evaluated σ_{GDR} (dashed lines) becomes smaller for the heavy nuclei. It seems such good reproduction of the resonance energy for the heavy nuclei is a common property of RPA calculations [59]. The peak cross sections in the FAM calculations are much smaller than those of evaluated data, σ_R . In the FAM calculations, we assume that the Lorentzian width γ is equal to

the width, Γ_R of recommended experimental GDR parameters in Ref. [51]. This assumption overestimates the value of γ and reduces the peak cross section in FAM calculations. The total width of GDR is given by the sum of three widths, $\Gamma_R = \Delta\Gamma + \Gamma^\uparrow + \Gamma^\downarrow$ where $\Delta\Gamma$, Γ^\uparrow , and Γ^\downarrow are the Landau damping, the escape width, and the spreading width, respectively [1, 4, 61]. The spreading width Γ^\downarrow represents the couplings of the 1p-1h states to more complex numerous configurations such as 2p-2h, and 3p-3h states [4]. The Lorentzian width γ can be regarded as Γ^\downarrow [29, 62]. Therefore, the total GDR width in FAM calculation, Γ_R^{FAM} should be larger than the Γ_R evaluated based on the experimental data when we assume $\gamma = \Gamma_R$. In the case of Fig. 2(d), for example, we can estimate the Γ_R^{FAM} by fitting the numerical result (solid line) with Eq. (47). We confirm that the $\Gamma_R^{\text{FAM}} = 5.9$ MeV is larger than $\gamma = 3.9$ MeV. Then, the damping width in the RPA is given by $\Delta\Gamma + \Gamma^\uparrow = 2.0$ MeV. In Fig. 3, we compare the FAM results for ^{208}Pb with different γ values. The $\gamma = 3.9$ MeV case in Fig. 3 is identical to Fig. 2(d). As γ decreases, the peak cross section (GDR width) increases (decreases). The energy-weighted sum rule is almost constant regardless the value of γ . In Fig. 3, the peak cross section of evaluated experimental data (dash line) is well reproduced by the FAM calculation of the $\gamma = 2.1$ MeV. The value of the $\Delta\Gamma + \Gamma^\uparrow$ might depend on the types of Skyrme forces because the sum rule enhancement factor, κ , is different depending on the type of Skyrme forces [63, 64]. A shoulder structure appears near 16 MeV, which is on the right-hand side of the resonance energy, when we employ the narrower Lorentzian width. The right shoulder of ^{208}Pb is also confirmed in the previous RPA calculation of the isovector strength function [65]. Such fragmentation of GDR might be universal for GDR of heavy nuclei irrespective of the nuclear shape [66].

3. Deformed nuclei

It is well known experimentally that the GDR peak splits into two for the statically deformed nuclei [3], because the degeneracy for different K values of 0, ± 1 is removed. As shown in Fig. 4, FAM reproduces the split of GDR for well-deformed nuclei such as ^{154}Sm and ^{238}U . The resonance energy of $K = 0$ is smaller than that of $K = \pm 1$ because of the longer wavelength along the axis of symmetry (z -axis), when the shape is prolate [4]. Because the pair correlations are no longer negligible for deformed nuclei, QRPA is commonly adopted to calculate GDRs of deformed nuclei [34, 62]. Although the pairing correlation is included in the single-particle states of HF+BCS, the particle and hole are chosen as fully unoccupied and occupied states above and below the Fermi surface given by BCS in our non-iterative FAM-RPA. This approximation results in some uncertainties in the transitions with very small excitation energies. Nevertheless, as shown in Fig. 4 by the solid lines, the FAM-RPA

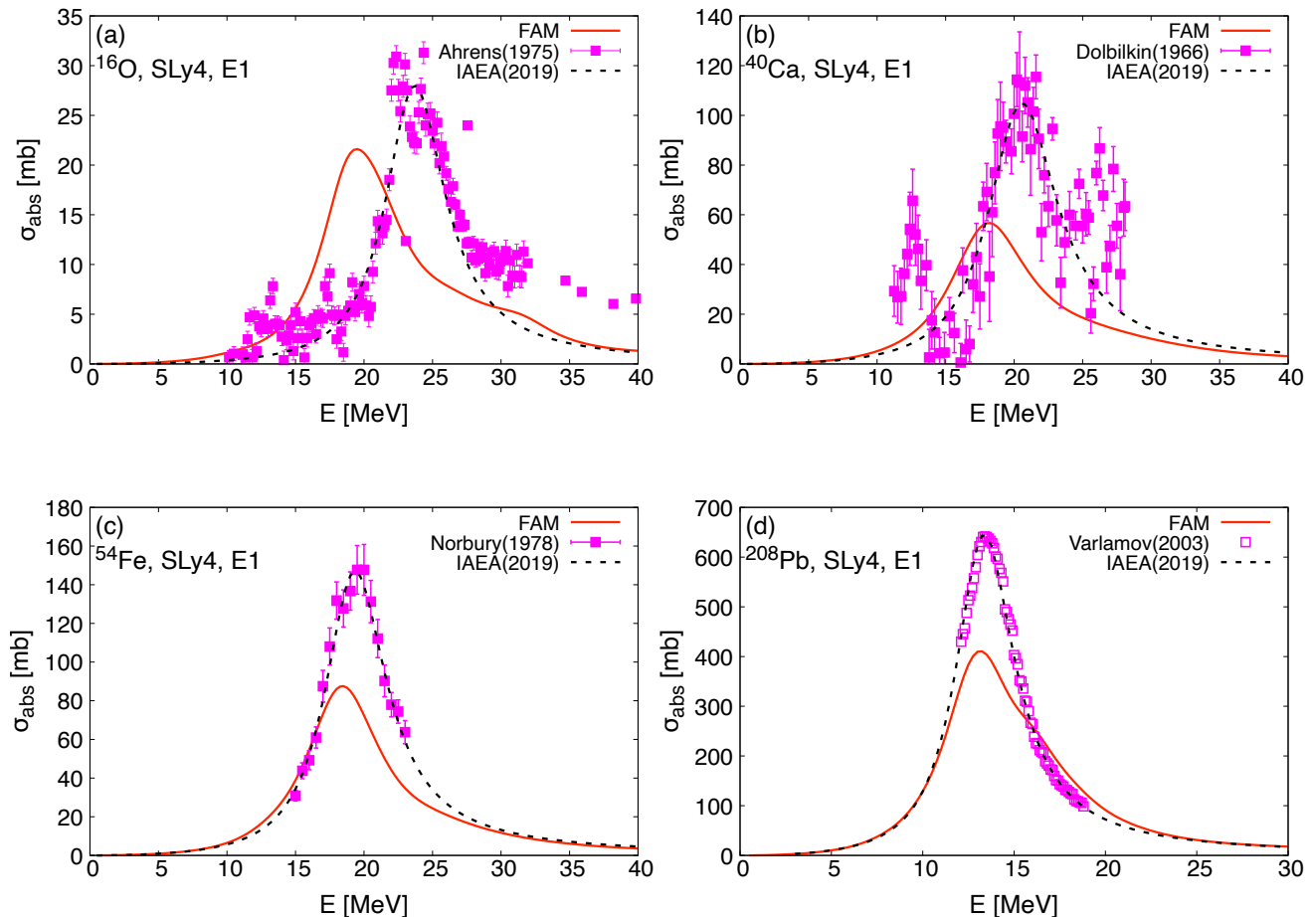


FIG. 2. The GDR cross sections for spherical nuclei, (a) ^{16}O , (b) ^{40}Ca , (c) ^{54}Fe , and (d) ^{208}Pb . The solid and dashed lines show the results of Eq. (42) and the evaluated σ_{GDR} in Eq. (47), respectively. The symbols represent both the reported and evaluated experimental data [54–57] in EXFOR [58].

calculations for $\sigma_{\text{abs}}(E, E_1)$ nicely reproduce the experimental data. This is because the E1 operator in Eq. (41) changes the parities of single-particle states, hence transitions within the same shells are strongly suppressed. These small energy transitions do not contribute to the main part of E1, even if we extend our model to FAM-QRPA, which is definitely planned.

In Fig. 4(a), our calculation predicts somewhat lower cross sections than the evaluated Lorentzian distribution, which is also seen in the QRPA calculation for ^{154}Sm where SLy4 is employed [62]. In both ^{154}Sm and ^{238}U , the second peak cross sections of FAM results are lower than the experimental data. This systematic disagreement occurs due to the Lorentzian width γ as we discussed before. The agreement on the second peak and the higher energy tail ($E > 16$ MeV) can be improved when a slightly smaller γ is used for $K = \pm 1$.

B. M1 transition

For the M1 transition, we use the magnetic dipole operator in Eq. (43) to perform almost the same calculation as done in Sec. III A. The value of the Lorentzian width is fixed to $\gamma = 1$ MeV. Here, we focus on the M1 transitions for double-magic nuclei.

Figure 5 shows the cross sections of M1 transitions for ^{48}Ca and ^{208}Pb . The transition strengths for $K = 0, \pm 1$ are almost identical. In the case of these double-magic nuclei, the spin part in Eq. (43) dominantly contributes to the transition strength of the M1 transitions.

The dominant peak around 8.5 MeV in Fig. 5(a) is originated from a spin-flip $1f_{7/2} \rightarrow 1f_{5/2}$ transition of neutrons [23]. As shown in Fig. 5(b), there are double peaks in the M1 transition of ^{208}Pb . These two peaks are not by the different K values but due to contributions from neutron spin-flip transitions and proton spin-flip transitions. The peak around 8.0 MeV (6.0 MeV) in Fig. 5(b) reflects the contribution from a spin-flip $1i_{13/2} \rightarrow 1i_{11/2}$ ($1h_{11/2} \rightarrow 1h_{9/2}$) transition of neutrons (protons), re-

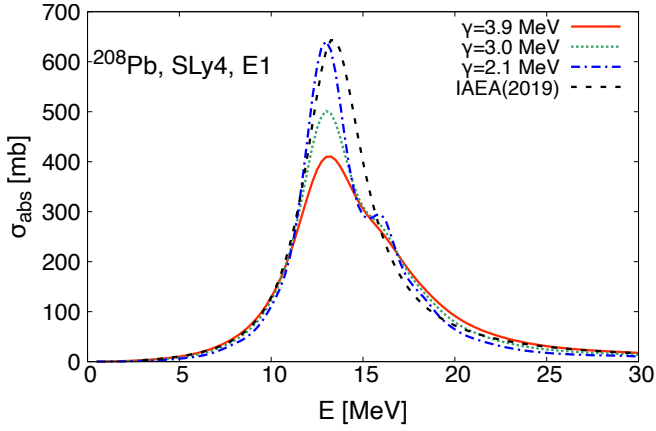


FIG. 3. The calculated GDR cross sections for ^{208}Pb with different Lorentzian width γ (solid, dotted, and dash-dotted lines) and the evaluated σ_{GDR} in Eq. (47) (dashed line). The result of $\gamma = 3.9$ MeV (solid line) corresponds to the FAM result in Fig. 2(d).

spectively. In our FAM calculations, the M1 transition strength distribution is given by

$$\frac{dB(\text{M1})}{dE} = \sum_{K=0,\pm 1} \frac{dB(E; M_K)}{dE}, \quad (48)$$

where the right hand side of the above equation is calculated from Eqs. (40) and (43). The results of such distributions for ^{48}Ca and ^{208}Pb are shown in the solid lines of Fig. 6. The strength distribution of ^{48}Ca is well consistent with that of Ref. [23]. On the other hand, experiments of inelastic scatterings such as $^{48}\text{Ca}(e, e')$ [69] and $^{48}\text{Ca}(p, p')$ [70] found a dominant peak of the M1 excitation at 10.23 MeV that is higher than the peak energy of 8.5 MeV in Fig. 5(a). As shown in Fig. 6, the results of M1 transitions with the residual interactions (solid lines) are identical to those without residual interactions (dot lines), which indicates residual interactions in Eqs. (32) and (39) do not contribute to the M1 transitions. Here, we employ SLy4 as the Skyrme force that ignores the contribution from the spin terms with $\tilde{b}_i, \tilde{b}'_i$ [18, 19]. These spin terms may increase the repulsive effects of residual interactions and upshift the peak energy of the M1 transitions.

Figure 6(b) shows the double-peak feature of M1 for ^{208}Pb , which is also confirmed by other theoretical works in the past, nevertheless the experimental data show only one peak near 7.3 MeV [70]. Such discrepancy could be attributed to theoretical uncertainty in Skyrme parameters, because some other works, which adopt different Skyrme parameterizations (e.g. SkO and SkO'), reported single peak shapes [18, 19]. The result of the M1 transition is more sensitive to the Skyrme parameterization than that of the E1 transition.

The total transition strength $\sum B(\text{M1})$ is commonly used to compare calculated results with experimental

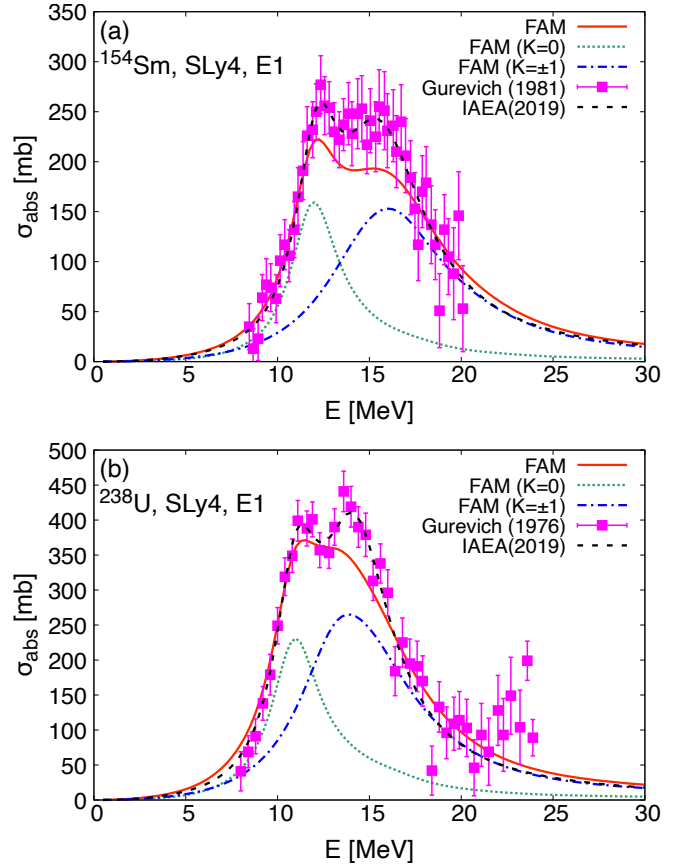


FIG. 4. The GDR cross sections for deformed nuclei, (a) ^{154}Sm and (b) ^{238}U . The partial contributions from $dB(E, D_0)/dE$ and $\sum_{K=\pm 1} dB(E, D_K)/dE$ in Eq. (42) are shown by the dotted and dash-dotted lines. The symbols represent the experimental data [67, 68].

data. In our FAM-RPA calculation, the total strength can be estimated from the integration of Eq. (48) over the energy E ,

$$\sum B(\text{M1}) = \int dE \frac{dB(\text{M1})}{dE}, \quad (49)$$

and they are $11.7 \mu_N^2 (32.5 \mu_N^2)$ for $^{48}\text{Ca} (^{208}\text{Pb})$, which are larger than the experimental data, e.g., $3.85 - 4.63 \mu_N^2 (20.5 \mu_N^2)$ for $^{48}\text{Ca} (^{208}\text{Pb})$ [70]. It is also reported that the calculated M1 transition in the past tends to give larger $\sum B(\text{M1})$ (e.g. [1] and references therein), and they suggested to introduce the quench of the spin g factors. The spin-flip part is dominant in the M1 transitions of double-magic nuclei so that the total strength in Eq. (49) is almost proportional to the square of the quenching factor. By introducing a typical value of the quenching factor, $g_{s,\text{eff}}^{(i)}/g_s^{(i)} = 0.6 - 0.7$ [23], the total strength in our FAM calculations is reduced by 0.36 - 0.49 times and more consistent with the experimental data [70].

When the nucleus is strongly deformed like nuclei in

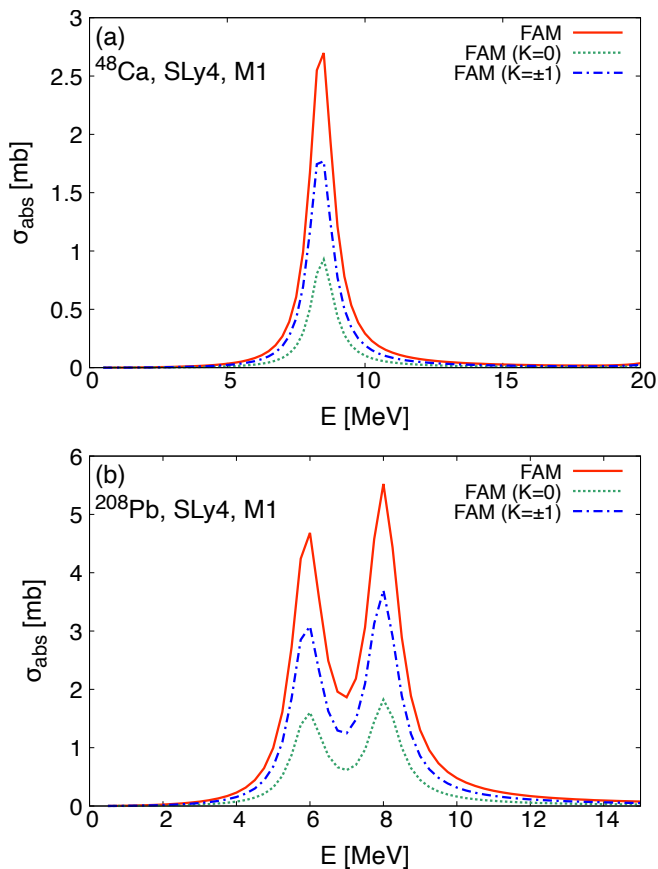


FIG. 5. The photoabsorption cross sections of M1 transitions for double-magic nuclei, (a) ^{48}Ca and (b) ^{208}Pb . The solid lines show the results of Eq. (44). The partial contributions from $K = 0$ and $K = \pm 1$ to the total strength are shown by the dotted and dash-dotted lines.

the rare-earth or actinide region, the so-called scissors mode may appear near 3 MeV [71], which comes from the orbital part in Eq. (43). They are very sensitive to the low-excitation configurations near the Fermi surface, and unfortunately our current implementation of non-iterative FAM-RPA brings a large uncertainty in calculating the scissors mode. This issue could be resolved by our next modeling of non-iterative FAM-QRPA.

IV. CONCLUSION

We develop a non-iterative FAM method, where the forward and backward amplitudes are derived from the explicit linearization of the residual interaction without an iterative procedure used in the other conventional FAM-RPA calculations. We carried out the HF+BCS calculation to prepare the ground state of the static HF Hamiltonian, then the occupied and unoccupied states are fed into the calculation of the E1 transitions for both the spherical and deformed nuclei. Our calculated result indicates that the E1 transition is not so sensitive to the

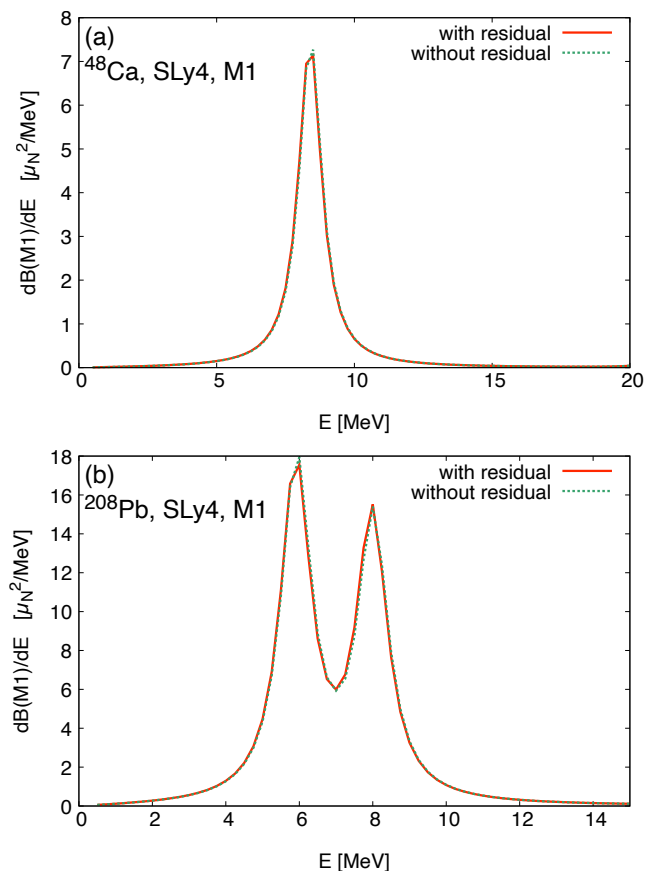


FIG. 6. The transition strength distributions in Eq. (48) for (a) ^{48}Ca and (b) ^{208}Pb . The solid (dotted) line shows the result with (without) the residual interactions in Eqs. (32) and (39).

detail of the single-particle states near the Fermi surface.

We also applied our FAM-RPA calculations to the M1 transitions for double-magic nuclei and demonstrated that the spin-flip of neutrons and protons is the main contribution to the M1 transition. FAM-RPA tends to overestimate the M1 transition strength, which might be resolved when we introduce quenching of the spin g factor. We also discussed the sensitivity of the spin term in the Skyrme force to the M1 transition, which is currently neglected in our calculations. This could shift the M1 resonance location higher, making our calculations more consistent with the experimental data.

ACKNOWLEDGMENTS

This work was partially supported by the Office of Defense Nuclear Nonproliferation Research & Development (DNN R&D), National Nuclear Security Administration, U.S. Department of Energy. This work was carried out under the auspices of the National Nuclear Security Administration of the U.S. Department of Energy at Los Alamos National Laboratory under Contract

$$\Lambda_\mu^\pm = \Omega_\mu \pm \frac{1}{2}, \quad (\text{A2})$$

Appendix A: Integrands in the residual interaction

We show the detailed description of integrands inside Eqs. (32) and (39). To prepare the HF single-particle state for the FAM-RPA calculation, we carry out the HF+BCS calculation as done in Ref. [49]. The HF single-particle state on the right-hand sides of Eqs. (13) and (14) is described in the cylindrical coordinate space $\vec{r} = (r, \varphi, z)$ [48],

$$\phi_\mu^q = \chi_q(\tau) \left\{ \frac{e^{i\Lambda_\mu^- \varphi}}{\sqrt{2\pi}} \phi_\mu^+(r, z) \chi_{1/2}(\sigma) + \frac{e^{i\Lambda_\mu^+ \varphi}}{\sqrt{2\pi}} \phi_\mu^-(r, z) \chi_{-1/2}(\sigma) \right\}, \quad (\text{A1})$$

where $\sigma(\tau)$ represents the spin (isospin) of the nucleon. $\chi_q(\tau)$ is the eigenstate of the isospin operator τ_z and the index q labels neutrons or protons. The $\chi_{1/2}(\sigma)$ and $\chi_{-1/2}(\sigma)$ represent the up and down states of the nucleon spin, respectively. The wave function $\phi_\mu^\pm(r, z)$ is expanded by the cylindrical harmonic oscillator basis. The Ω_μ represents the projection of the total angular momentum on z -axis. The integrands such as $\phi_m^{q*} \phi_i^q$, $\vec{\nabla} \phi_m^{q*} \vec{\nabla} \phi_i^q$, $\phi_m^{q*} \nabla^2 \phi_i^q$, and $(-i) \vec{\nabla} \phi_m^{q*} (\vec{\nabla} \times \vec{\sigma}) \phi_i^q$ in Eq. (32) are described in the cylindrical coordinate (r, φ, z) . The spin and isospin states inside these integrands are eliminated owing to the inner products, $\chi_{\Sigma'}^\dagger(\sigma) \chi_\Sigma(\sigma) = \delta_{\Sigma\Sigma'}$ ($\Sigma, \Sigma' = \pm 1/2$) and $\chi_q^\dagger(\tau) \chi_q(\tau) = 1$. Similar to the detailed calculation of local densities and currents in Ref. [48], the integrand functions in the residual interaction of the time-even Hamiltonian are written as

$$\phi_m^{q*} \phi_i^q = \frac{e^{i(\Omega_i - \Omega_m)\varphi}}{2\pi} (\phi_m^+ \phi_i^+ + \phi_m^- \phi_i^-), \quad (\text{A3})$$

$$\vec{\nabla} \phi_m^{q*} \cdot \vec{\nabla} \phi_i^q = \frac{e^{i(\Omega_i - \Omega_m)\varphi}}{2\pi} \left\{ \nabla_r \phi_m^+ \nabla_r \phi_i^+ + \nabla_z \phi_m^+ \nabla_z \phi_i^+ + \frac{\Lambda_m^- \Lambda_i^-}{r^2} \phi_m^+ \phi_i^+ + \nabla_r \phi_m^- \nabla_r \phi_i^- + \nabla_z \phi_m^- \nabla_z \phi_i^- + \frac{\Lambda_m^+ \Lambda_i^+}{r^2} \phi_m^- \phi_i^- \right\}, \quad (\text{A4})$$

$$\phi_m^{q*} \nabla^2 \phi_i^q = \frac{e^{i(\Omega_i - \Omega_m)\varphi}}{2\pi} \left\{ \phi_m^+ \left[\frac{1}{r} \nabla_r (r \nabla_r) + \nabla_z^2 - \frac{(\Lambda_i^-)^2}{r^2} \right] \phi_i^+ + \phi_m^- \left[\frac{1}{r} \nabla_r (r \nabla_r) + \nabla_z^2 - \frac{(\Lambda_i^+)^2}{r^2} \right] \phi_i^- \right\}, \quad (\text{A5})$$

$$(-i) \vec{\nabla} \phi_m^{q*} \cdot (\vec{\nabla} \times \vec{\sigma}) \phi_i^q = \frac{e^{i(\Omega_i - \Omega_m)\varphi}}{2\pi} \left\{ \nabla_r \phi_i^+ \nabla_z \phi_m^- - \nabla_r \phi_i^- \nabla_z \phi_m^+ + \nabla_r \phi_m^+ \nabla_z \phi_i^- - \nabla_r \phi_m^- \nabla_z \phi_i^+ + \frac{\Lambda_m^-}{r} \phi_m^+ (\nabla_r \phi_i^+ - \nabla_z \phi_i^-) + \frac{\Lambda_i^-}{r} \phi_i^+ (\nabla_r \phi_m^+ - \nabla_z \phi_m^-) - \frac{\Lambda_m^+}{r} \phi_m^- (\nabla_r \phi_i^- + \nabla_z \phi_i^+) - \frac{\Lambda_i^+}{r} \phi_i^- (\nabla_r \phi_m^- + \nabla_z \phi_m^+) \right\}, \quad (\text{A6})$$

where we use simple notations, $\nabla_{r(z)} \equiv \partial/\partial r(z)$ and $\phi_\mu^\pm \equiv \phi_\mu^\pm(r, z)$. The operator $(\vec{\nabla} \times \vec{\sigma})$ in Eq. (A6) is described in the cylindrical coordinate. $\vec{\sigma}$ operates the spin eigenstates as in $\sigma_\pm \chi_{\pm 1/2} = 0$, $\sigma_\pm \chi_{\mp 1/2} = 2\chi_{\pm 1/2}$, and $\sigma_z \chi_{\pm 1/2} = \pm \chi_{\pm 1/2}$. The ϕ_μ^\pm is a real number function in the (r, z) space. The detailed description of $\nabla_{r(z)} \phi_\mu^\pm$ is shown in Ref. [48]. All of the φ dependence is summarized into the factor $e^{i(\Omega_i - \Omega_m)\varphi}$ in Eqs. (A3)-(A6). The spatial integrals in Eq. (32) are carried out in the cylindrical coordinate (r, φ, z) . The integration towards the φ direction induces a condition, $\Omega_i - \Omega_m = \Omega_j - \Omega_n$

for the finite value of Eq. (32). Such a condition of angular momentum restricts the size of the RPA matrix A . In the case of the RPA matrix B , the condition becomes $\Omega_i - \Omega_m = -(\Omega_j - \Omega_n)$, where the negative sign on the right-hand side comes from the relation in Eq. (29). The integrands in Eq. (32) can be expanded by a linear combination of Hermite (associated Laguerre) polynomials in the $z(r)$ direction by following the formalism in Ref. [48]. The spatial integrations over z and r directions in Eq. (32) can be carried out by the Gaussian quadratures. In the case of the time-odd Hamiltonian,

the residual interaction in Eq. (39) includes two types of vectors, $\vec{\nabla} \times (\phi_m^{q*} \vec{\sigma} \phi_i^q)$ and $\frac{1}{2i}(\phi_m^{q*} \vec{\nabla} \phi_i^q - \phi_i^q \vec{\nabla} \phi_m^{q*})$. In the

cylindrical coordinate, the components of these vectors are written as

$$\begin{aligned} \left\{ \vec{\nabla} \times (\phi_m^{q*} \vec{\sigma} \phi_i^q) \right\}_r &= \frac{e^{i(\Omega_i - \Omega_m)\varphi}}{2\pi} i \left\{ \frac{\Omega_i - \Omega_m}{r} (\phi_m^+ \phi_i^+ - \phi_m^- \phi_i^-) - \nabla_z (-\phi_m^+ \phi_i^- + \phi_m^- \phi_i^+) \right\}, \\ \left\{ \vec{\nabla} \times (\phi_m^{q*} \vec{\sigma} \phi_i^q) \right\}_\varphi &= \frac{e^{i(\Omega_i - \Omega_m)\varphi}}{2\pi} \left\{ \nabla_z (\phi_m^+ \phi_i^- + \phi_m^- \phi_i^+) - \nabla_r (\phi_m^+ \phi_i^+ - \phi_m^- \phi_i^-) \right\}, \\ \left\{ \vec{\nabla} \times (\phi_m^{q*} \vec{\sigma} \phi_i^q) \right\}_z &= \frac{e^{i(\Omega_i - \Omega_m)\varphi}}{2\pi} i \left\{ -\frac{\Omega_i - \Omega_m}{r} (\phi_m^+ \phi_i^- + \phi_m^- \phi_i^+) + (\nabla_r + \frac{1}{r}) (-\phi_m^+ \phi_i^- + \phi_m^- \phi_i^+) \right\}, \end{aligned} \quad (\text{A7})$$

$$\begin{aligned} \frac{1}{2i} (\phi_m^{q*} \vec{\nabla} \phi_i^q - \phi_i^q \vec{\nabla} \phi_m^{q*})_r &= \frac{e^{i(\Omega_i - \Omega_m)\varphi}}{2\pi} \frac{1}{2i} (\phi_m^+ \nabla_r \phi_i^+ - \phi_i^+ \nabla_r \phi_m^+ + \phi_m^- \nabla_r \phi_i^- - \phi_i^- \nabla_r \phi_m^-), \\ \frac{1}{2i} (\phi_m^{q*} \vec{\nabla} \phi_i^q - \phi_i^q \vec{\nabla} \phi_m^{q*})_\varphi &= \frac{e^{i(\Omega_i - \Omega_m)\varphi}}{2\pi} \frac{1}{2} \left(\frac{\Omega_m + \Omega_i - 1}{r} \phi_m^+ \phi_i^+ + \frac{\Omega_m + \Omega_i + 1}{r} \phi_m^- \phi_i^- \right), \\ \frac{1}{2i} (\phi_m^{q*} \vec{\nabla} \phi_i^q - \phi_i^q \vec{\nabla} \phi_m^{q*})_z &= \frac{e^{i(\Omega_i - \Omega_m)\varphi}}{2\pi} \frac{1}{2i} (\phi_m^+ \nabla_z \phi_i^+ - \phi_i^+ \nabla_z \phi_m^+ + \phi_m^- \nabla_z \phi_i^- - \phi_i^- \nabla_z \phi_m^-), \end{aligned} \quad (\text{A8})$$

where the dependence of φ is included in the factor $e^{i(\Omega_i - \Omega_m)\varphi}$. As in the case of the time-even Hamiltonian, $\Omega_i - \Omega_m = \Omega_j - \Omega_n$ is necessary for the finite value of the residual interaction in Eq. (39).

Appendix B: Calculation of the Coulomb potential

The contribution from the direct term of the Coulomb potential in Eq. (32) is written as

$$\begin{aligned} (\tilde{V}_C)_{nj} &= \frac{e^2}{2} \int d^3 r' \frac{\phi_j^{p*} \phi_n^p}{|\vec{r} - \vec{r}'|} \\ &= \frac{e^2}{4} \int d^3 r' |\vec{r} - \vec{r}'| \nabla'^2 (\phi_j^{p*} \phi_n^p), \end{aligned} \quad (\text{B1})$$

where the relation $\nabla'^2 |\vec{r} - \vec{r}'| = 2/|\vec{r} - \vec{r}'|$ is used. Then, we carry out the integration by parts twice. Eq. (B1) is a function in the cylindrical coordinate (r, φ, z) . The integration can be described by following the procedure to calculate the Coulomb potential in Ref. [48],

$$\begin{aligned} (\tilde{V}_C)_{nj} &= \frac{e^{i(\Omega_n - \Omega_j)\varphi}}{2\pi} e^2 \int_0^\infty dr' \int_{-\infty}^\infty dz' \\ &\quad \times \left\{ \sqrt{(r+r')^2 + (z-z')^2} J(r', z') I(\Omega_n - \Omega_j, x) \right\}, \end{aligned} \quad (\text{B2})$$

$$J(r', z') = (2\pi) e^{-i(\Omega_n - \Omega_j)\varphi'} \nabla'^2 (\phi_j^{p*} \phi_n^p), \quad (\text{B3})$$

$$I(x, \Omega) = (-1)^\Omega \int_0^{\pi/2} d\varphi' \sqrt{1 - x^2 \sin^2 \varphi'} \cos(2\Omega\varphi'), \quad (\text{B4})$$

$$x^2 = \frac{4rr'}{\sqrt{(r+r')^2 + (z-z')^2}}, \quad (\text{B5})$$

where the factor $e^{-i(\Omega_n - \Omega_j)\varphi'}$ in Eq. (B3) cancels the φ' dependence in $\nabla'^2 (\phi_j^{p*} \phi_n^p)$ that is calculated from Eqs. (A4) and (A5). The difference in angular momentum is restricted to $|\Omega_n - \Omega_j| = 0, 1$ when the external fields are the operators of E1 and M1 transitions. At $\Omega = 0$, Eq. (B4) corresponds to the well-known complete elliptic integral of the second kind. After the Taylor expansion and term by term integration, Eq. (B4) at $\Omega = 0, \pm 1$ can be expressed by the infinite power series,

$$I(x, \Omega = 0) = \frac{\pi}{2} \sum_{n=0}^\infty \left\{ \frac{(2n-1)!!}{(2n)!!} \right\}^2 \frac{x^{2n}}{1-2n}, \quad (\text{B6})$$

$$I(x, \Omega = \pm 1) = \frac{\pi}{2} \sum_{n=0}^\infty \left\{ \frac{(2n-1)!!}{(2n)!!} \right\}^2 \frac{n}{(n+1)(1-2n)} x^{2n}, \quad (\text{B7})$$

where $(-1)!! \equiv 1$. This expansions for $x^2 < 1$ converge sufficiently when $n = 10$ or higher.

Appendix C: Coefficients of the external fields

In the case of E1 transition, the coefficient f_{mi}^q in Eq. (19) is calculated by

$$\begin{aligned} f_{mi}^q &= \int d^3r \phi_m^{q*} \sum_{K=0,\pm 1} D_K \phi_i^q \\ &= \sqrt{\frac{3}{4\pi}} \int_0^\infty dr r \int_{-\infty}^\infty dz g^{E1}(\Omega_{mi}, q), \end{aligned} \quad (C1)$$

$$g^{E1}(\Omega_{mi}, q) = \begin{cases} z e_{\text{eff}}^q (\phi_m^+ \phi_i^+ + \phi_m^- \phi_i^-) & (\Omega_{mi} = 0) \\ \mp \frac{r}{\sqrt{2}} e_{\text{eff}}^q (\phi_m^+ \phi_i^+ + \phi_m^- \phi_i^-) & (\Omega_{mi} = \pm 1) \\ 0 & (\text{otherwise}) \end{cases}, \quad (C2)$$

where $\Omega_{mi} \equiv \Omega_m - \Omega_i$ and $e_{\text{eff}}^q \equiv -eZ/A(eN/A)$ for $q = n(p)$. The condition of Ω_{mi} comes from the integration over φ , which restricts the size of the configuration space. We can derive the coefficient f_{im}^q in Eq. (19) in the same way. In the case of M1 transition, the operator $\vec{\sigma}$ can flip

the spin of nucleons. The coefficient f_{mi}^q is given by

$$f_{mi}^q = \int d^3r \phi_m^{q*} \sum_{K=0,\pm 1} M_K \phi_i^q \quad (C3)$$

$$= \sqrt{\frac{3}{4\pi}} \int_0^\infty dr r \int_{-\infty}^\infty dz g^{M1}(\Omega_{mi}, q), \quad (C4)$$

where the $g^{M1}(\Omega_{mi}, q)$ is finite only for $\Omega_{mi} = 0, \pm 1$ as in Eq. (C2). The detailed description of the function $g^{M1}(\Omega_{mi}, q)$ is written as

$$\begin{aligned} g^{M1}(0, q) &= \mu_N g_l^q (\Lambda_i^- \phi_m^+ \phi_i^+ + \Lambda_i^+ \phi_m^- \phi_i^-) \\ &\quad + \frac{\mu_N g_s^q}{2} (\phi_m^+ \phi_i^+ - \phi_m^- \phi_i^-), \end{aligned} \quad (C5)$$

$$\begin{aligned} g^{M1}(1, q) &= \frac{\mu_N g_l^q}{\sqrt{2}} \phi_m^+ (-z \nabla_r + r \nabla_z) \phi_i^+ \\ &\quad + \frac{\mu_N g_l^q}{\sqrt{2}} \phi_m^- (-z \nabla_r + r \nabla_z) \phi_i^- \\ &\quad + \frac{\mu_N g_l^q}{\sqrt{2}} \frac{z}{r} (\Lambda_i^- \phi_m^+ \phi_i^+ + \Lambda_i^+ \phi_m^- \phi_i^-) - \frac{\mu_N g_s^q}{\sqrt{2}} \phi_m^+ \phi_i^-, \end{aligned} \quad (C6)$$

$$\begin{aligned} g^{M1}(-1, q) &= \frac{\mu_N g_l^q}{\sqrt{2}} \phi_m^+ (-z \nabla_r + r \nabla_z) \phi_i^+ \\ &\quad + \frac{\mu_N g_l^q}{\sqrt{2}} \phi_m^- (-z \nabla_r + r \nabla_z) \phi_i^- \\ &\quad - \frac{\mu_N g_l^q}{\sqrt{2}} \frac{z}{r} (\Lambda_i^- \phi_m^+ \phi_i^+ + \Lambda_i^+ \phi_m^- \phi_i^-) + \frac{\mu_N g_s^q}{\sqrt{2}} \phi_m^- \phi_i^+, \end{aligned} \quad (C7)$$

where $g_s^q = -3.826(5.586)$ and $g_l^q = 0(1)$ for $q = n(p)$.

-
- [1] M. Harakeh and A. Woude, *Giant Resonances: Fundamental High-frequency Modes of Nuclear Excitation* (Oxford University Press, 2001).
- [2] W. Bothe and W. Gentner, *Zeitschrift fur Physik* **106**, 236 (1937).
- [3] B. L. Berman and S. C. Fultz, *Rev. Mod. Phys.* **47**, 713 (1975).
- [4] J. Speth and A. van der Woude, *Reports on Progress in Physics* **44**, 719 (1981).
- [5] S. Goriely, E. Khan, and M. Samyn, *Nucl. Phys. A* **739**, 331 (2004).
- [6] M. R. Mumpower, T. Kawano, J. L. Ullmann, M. Kr̄tička, and T. M. Sprouse, *Phys. Rev. C* **96**, 024612 (2017).
- [7] D. M. Brink, unpublished D. Phil. thesis, Oxford University (1955).
- [8] M. R. Mumpower, R. Surman, G. C. McLaughlin, and A. Aprahamian, *Prog. Part. Nucl. Phys.* **86**, 86 (2016).
- [9] T. Kajino, W. Aoki, A. B. Balantekin, R. Diehl, M. A. Famiano, and G. J. Mathews, *Prog. Part. Nucl. Phys.* **107**, 109 (2019).
- [10] J. J. Cowan, C. Sneden, J. E. Lawler, A. Aprahamian, M. Wiescher, K. Langanke, G. Martínez-Pinedo, and F.-K. Thielemann, *Rev. Mod. Phys.* **93**, 15002 (2021).
- [11] C. Fröhlich, G. Martínez-Pinedo, M. Liebendörfer, F.-K. Thielemann, E. Bravo, W. R. Hix, K. Langanke, and N. T. Zinner, *Phys. Rev. Lett.* **96**, 142502 (2006).
- [12] H. Sasaki, T. Kajino, T. Takiwaki, T. Hayakawa, A. B. Balantekin, and Y. Pehlivan, *Phys. Rev. D* **96**, 043013 (2017).
- [13] H. Sasaki, Y. Yamazaki, T. Kajino, M. Kusakabe, T. Hayakawa, M.-K. Cheoun, H. Ko, and G. J. Mathews, *Astrophys. J.* **924**, 29 (2022).
- [14] P. Ring and P. Schuck, *The Nuclear Many-Body Problem*, Physics and astronomy online library (Springer, 2004).
- [15] D. Rowe, *Nuclear Collective Motion: Models and Theory* (World Scientific, 2010).
- [16] T. Nakatsukasa, K. Matsuyanagi, M. Matsuo, and K. Yabana, *Rev. Mod. Phys.* **88**, 045004 (2016).
- [17] G. Colò, *arXiv:2201.04578* (2022).

- [18] P. Vesely, J. Kvasil, V. O. Nesterenko, W. Kleinig, P. G. Reinhard, and V. Y. Ponomarev, *Phys. Rev. C* **80**, 031302 (2009).
- [19] V. O. Nesterenko, J. Kvasil, P. Vesely, W. Kleinig, P. G. Reinhard, and V. Y. Ponomarev, *J. Phys. G* **37**, 064034 (2010).
- [20] L.-G. Cao, G. Colò, H. Sagawa, P. F. Bortignon, and L. Sciacchitano, *Phys. Rev. C* **80**, 064304 (2009).
- [21] S. Goriely, S. Hilaire, S. Péru, M. Martini, I. Deloncle, and F. Lechaftois, *Phys. Rev. C* **94**, 044306 (2016).
- [22] V. Tselyaev, N. Lyutorovich, J. Speth, P. G. Reinhard, and D. Smirnov, *Phys. Rev. C* **99**, 064329 (2019).
- [23] G. Kruzić, T. Oishi, D. Vale, and N. Paar, *Phys. Rev. C* **102**, 044315 (2020).
- [24] T. Oishi, G. Kruzić, and N. Paar, *J. Phys. G* **47**, 115106 (2020).
- [25] V. O. Nesterenko, P. I. Vishnevskiy, J. Kvasil, A. Repko, and W. Kleinig, *Phys. Rev. C* **103**, 064313 (2021).
- [26] S. Ebata, T. Nakatsukasa, T. Inakura, K. Yoshida, Y. Hashimoto, and K. Yabana, *Phys. Rev. C* **82**, 034306 (2010).
- [27] I. Stetcu, A. Bulgac, P. Magierski, and K. J. Roche, *Phys. Rev. C* **84**, 051309 (2011).
- [28] T. Nakatsukasa, T. Inakura, and K. Yabana, *Phys. Rev. C* **76**, 024318 (2007).
- [29] T. Inakura, T. Nakatsukasa, and K. Yabana, *Phys. Rev. C* **80**, 044301 (2009).
- [30] P. Avogadro and T. Nakatsukasa, *Phys. Rev. C* **84**, 014314 (2011).
- [31] M. Stoitsov, M. Kortelainen, T. Nakatsukasa, C. Losa, and W. Nazarewicz, *Phys. Rev. C* **84**, 041305 (2011).
- [32] N. Hinohara, M. Kortelainen, and W. Nazarewicz, *Phys. Rev. C* **87**, 064309 (2013).
- [33] M. Kortelainen, N. Hinohara, and W. Nazarewicz, *Phys. Rev. C* **92**, 051302 (2015).
- [34] T. Oishi, M. Kortelainen, and N. Hinohara, *Phys. Rev. C* **93**, 034329 (2016).
- [35] H. Liang, T. Nakatsukasa, Z. Niu, and J. Meng, *Phys. Rev. C* **87**, 054310 (2013).
- [36] T. Nikšić, N. Kralj, T. Tutiš, D. Vretenar, and P. Ring, *Phys. Rev. C* **88**, 044327 (2013).
- [37] P. Avogadro and T. Nakatsukasa, *Phys. Rev. C* **87**, 014331 (2013).
- [38] M. T. Mustonen, T. Shafer, Z. Zenginerler, and J. Engel, *Phys. Rev. C* **90**, 024308 (2014).
- [39] T. Shafer, J. Engel, C. Fröhlich, G. C. McLaughlin, M. Mumpower, and R. Surman, *Phys. Rev. C* **94**, 055802 (2016).
- [40] E. M. Ney, J. Engel, T. Li, and N. Schunck, *Phys. Rev. C* **102**, 034326 (2020).
- [41] N. Hinohara and J. Engel, [arXiv:2201.12983](https://arxiv.org/abs/2201.12983) (2022).
- [42] K. Washiyama, N. Hinohara, and T. Nakatsukasa, *Phys. Rev. C* **103**, 014306 (2021).
- [43] Y. M. Engel, D. M. Brink, K. Goeke, S. J. Krieger, and D. Vautherin, *Nucl. Phys. A* **249**, 215 (1975).
- [44] J. Dobaczewski and J. Dudek, *Phys. Rev. C* **52**, 1827 (1995).
- [45] J. A. Maruhn, P. G. Reinhard, P. D. Stevenson, and A. S. Umar, *Comput. Phys. Commun.* **185**, 2195 (2014).
- [46] S. Jin, K. J. Roche, I. Stetcu, I. Abdurrahman, and A. Bulgac, *Comput. Phys. Commun.* **269**, 108130 (2021).
- [47] E. Chabanat, P. Bonche, P. Haensel, J. Meyer, and R. Schaeffer, *Nucl. Phys. A* **635**, 231 (1998).
- [48] D. Vautherin, *Phys. Rev. C* **7**, 296 (1973).
- [49] L. Bonneau, T. Kawano, T. Watanabe, and S. Chiba, *Phys. Rev. C* **75**, 054618 (2007).
- [50] P. Möller, A. J. Sierk, T. Ichikawa, and H. Sagawa, *Atom. Data Nucl. Data Tabl.* **109-110**, 1 (2016).
- [51] T. Kawano, Y. Cho, P. Dimitriou, D. Filipescu, N. Iwamoto, V. Plujko, X. Tao, H. Utsunomiya, V. Varlamov, R. Xu, R. Capote, I. Gheorghe, O. Gorbachenko, Y. Jin, T. Renstrøm, M. Sin, K. Stopani, Y. Tian, G. Tveten, J. Wang, T. Belgya, R. Firestone, S. Goriely, J. Kopecky, M. Krťicka, R. Schwengner, S. Siem, and M. Wiedeking, *Nucl. Data Sheets* **163**, 109 (2020).
- [52] J. S. Levinger, *Physics Letters B* **82**, 181 (1979).
- [53] M. B. Chadwick, P. Obložinský, P. E. Hodgson, and G. Reffo, *Phys. Rev. C* **44**, 814 (1991).
- [54] J. Ahrens, H. Borchert, K. H. Czock, H. B. Epler, H. Gimm, H. Gundry, M. Kröning, P. Riehn, G. Sita Ram, A. Zieger, and B. Ziegler, *Nuclear Physics, Section A* **251**, 479 (1975).
- [55] B. S. Dolbilkin, V. A. Zapevalov, V. I. Korin, L. E. Lazareva, and F. A. Nikolaev, *Bull. Russian Academy of Sciences - Physics* **30**, 354 (1966).
- [56] J. W. Norbury, M. N. Thompson, K. Shoda, and H. Tsubota, *Australian Journal of Physics* **31**, 471 (1978).
- [57] V. V. Varlamov, M. E. Stepanov, and V. V. Chesnokov, *Bull. Russian Academy of Sciences - Physics* **67**, 724 (2003).
- [58] V. A. Plujko, O. M. Gorbachenko, R. Capote, and P. Dimitriou, *Atom. Data Nucl. Data Tabl.* **123-124**, 1 (2018).
- [59] J. Erler, P. Klupfel, and P. G. Reinhard, *J. Phys. G* **37**, 064001 (2010).
- [60] W. D. Myers, W. J. Swiatecki, T. Kodama, L. J. El-Jaick, and E. R. Hilf, *Phys. Rev. C* **15**, 2032 (1977).
- [61] J. Wambach, *Reports on Progress in Physics* **51**, 989 (1988).
- [62] K. Yoshida and T. Nakatsukasa, *Phys. Rev. C* **83**, 021304 (2011).
- [63] M. Bender, P.-H. Heenen, and P.-G. Reinhard, *Rev. Mod. Phys.* **75**, 121 (2003).
- [64] P. Klupfel, P. G. Reinhard, T. J. Burvenich, and J. A. Maruhn, *Phys. Rev. C* **79**, 034310 (2009).
- [65] V. O. Nesterenko, J. Kvasil, and P. G. Reinhard, *Phys. Rev. C* **66**, 044307 (2002).
- [66] V. O. Nesterenko, W. Kleinig, J. Kvasil, P. Vesely, and P. G. Reinhard, *Int. J. Mod. Phys. E* **16**, 624 (2007).
- [67] G. M. Gurevich, L. E. Lazareva, V. M. Mazur, S. Y. Merkulov, G. V. Solodukhov, and V. A. Tyutin, *Nuclear Physics, Section A* **351**, 257 (1981).
- [68] G. M. Gurevich, L. E. Lazareva, V. M. Mazur, G. V. Solodukhov, and B. A. Tulupov, *Nuclear Physics, Section A* **273**, 326 (1976).
- [69] W. Steffen, H. D. Gräf, W. Gross, D. Meuer, A. Richter, E. Spamer, O. Titze, and W. Knüpfer, *Physics Letters B* **95**, 23 (1980).
- [70] J. Birkhan, H. Matsubara, P. von Neumann-Cosel, N. Pietralla, V. Y. Ponomarev, A. Richter, A. Tamii, and J. Wambach, *Phys. Rev. C* **93**, 041302 (2016).
- [71] K. Heyde, P. von Neumann-Cosel, and A. Richter, *Rev. Mod. Phys.* **82**, 2365 (2010).